Some aspects of interface adhesion of electrolytically oxidized carbon fibres in an epoxy-resin matrix

C. A. BAILLIE*, M. G. BADER
Department of Materials Science and Engineering, University of Surrey, Guildford, Surrey GU2 5XH, UK

A comprehensive investigation of the adhesion at the interface of a carbon fibre in an epoxy resin was made. The fibre surfaces were modified, to increase their adhesion to resin, by an electrolytic surface treatment which was applied at various current densities. Subsequent changes in the fibre properties relating to possible mechanical, physical and chemical contributions to adhesion were monitored. Tensile tests on single fibres indicated that the treatment altered the strengths of the fibres, which were found to have their highest values and to be least variable at an optimum adhesion level. A method was developed to estimate the strength of the fibres in the resin, this confirmed the single-fibre data. A novel method of labelling the acidic sites by producing adsorption isotherms was developed to identify surface functionality. Surface acidity correlated well with adhesion levels. Single-fibre pull-out tests, modelled using a new combination failure criterion and fragmentation tests, indicated that the optimum adhesion level for this fibre/resin system was achieved with an electrolytic treatment at 25 C m^{-2}. The principal effects of this treatment were considered to be due to chemical modification of the fibre surface coupled with the removal of a loosely adherent surface layer.

1. Introduction

The mechanical properties of a fibre-reinforced plastic are largely dependent on the interface between the two components. Strong adhesion improves the strength but it may reduce the toughness, optimization is therefore necessary. In carbon-fibre/epoxy composites the surface treatments are applied to the fibre in order to improve the adhesion to this optimum level. However the adhesion mechanisms and the changes at the fibre surface necessary to achieve the optimum bond and the mechanisms of adhesion are not well understood.

Many workers have studied this problem but usually only in one specific area. Different carbon fibres, surface treatments and resins have been studied, so that it is difficult to draw meaningful conclusions. An additional problem is that most of the systems investigated are commercial and therefore very little is revealed about the details of composition and processing. For these reasons the present work has been confined to the study of a single fibre/resin system.

A single spool of a high-strength carbon fibre was received untreated and unsized from the suppliers. It was then treated with increasing levels of a commercial-type electrolytic process. One resin/hardener system was supplied and the same batch was used for all experiments. The samples were cured under controlled conditions.

The next stage was to fully characterize the fibres and resin. Properties were considered which might contribute mechanically, physically or chemically to the bond strength. The mechanical factors considered included the flaw severity and distribution which also yielded information on the fibre strength for subsequent modelling work. Data from tensile tests of the fibres in free air were compared with results from fibres embedded in resin, measured by a new technique, employing fragmentation tests. Physical bonding will not be considered as it has been established [1] that there is not a great improvement in wetting with surface treatment. The chemical-bonding contributions were analysed by measuring the change in acidity and bonding potential of the fibre surface after increasing levels of treatment by a novel method which makes use of X-ray photoelectron spectroscopy (XPS) determined adsorption isotherms to determine the uptake of a labelling ion from solution.

The tests selected to study the interface were fragmentation and pull-out tests, both of which require analyses of the stress state in the model composite in order that values of the adhesive strength may be estimated. The pull-out test has been studied in terms of two failure criteria. One involves the maximum shear stress of the interface exceeding the interfacial-shear strength and the other considers debonding as crack propagation with an associated fracture toughness. A new model combining some features of both criteria is developed and applied to pull-out data in this paper. Interfacial properties for these fibres are

Present address, Department of Mechanical Engineering, University of Sydney, 2006 Australia.

then calculated. The range of fragment lengths from the fragmentation tests is a sensitive detector of changes at the interface, and simple models can be applied to generate a value of an average shear strength for the interface. These are then compared with results from pull-out tests.

2. Experimental procedure
2.1. Materials
The fibre used was a Courtaulds polyacrylonitrile-based (PAN-based) high-strength carbon fibre [Grafil XA] which was received untreated and unsized. This was electrolytically surface treated in an ammonium-bicarbonate electrolyte. The residence time of the fibres in the electrolyte was maintained constant, and the current density varied. The treatment is characterized by the total charge density ($C\,m^{-2}$). The fibres are thus designated U for untreated fibres and 1 to 100 for fibres treated at 1 to 100 $C\,m^{-2}$. The resin used was a Ciba Geigy DGEBA resin MY750 with 12% HY951 tetraamine hardener, cured at 60 °C for 3 h followed by curing at 120 °C for 2 h.

2.2. Fibre characterization
2.2.1. Fibre strength
Single-fibre tensile tests were carried out at all treatment levels. The data were analysed according to the Weibull two-parameter distribution. Fibre strength in resin was then estimated from data generated from fragmentation tests by a new adaptation of the Weibull model.

A method adopted for the determination of the tensile strength of the carbon fibres in air was based on the standard ASTM test method (ASTMD3379-75, 1982) for single filaments of a fixed gauge length. This technique was adapted by the use of a multi-window card which allowed three tests at gauge lengths of 12, 30 and 75 mm to be conducted on adjacent portions of a single fibre extracted from the tow: the technique was first used for a non-parametric test of the weak-link principle [2].

Up to 48 fibres of each gauge length were tested at each of the following treatment levels: U, 1, 3, 5, 10, 15, 25, 50, 75, 100 and 400. The failure stresses were calculated from the maximum load on the load–extension plot and a value of the cross-sectional area for each fibre. The latter values were determined from the diameters (measured using an image-shearing technique) and assuming a circular cross-section.

It is well-known that fibre tensile strengths may be treated by a Weibull-distribution function to provide a measure of the strength variability and the strength-to-length dependence. The distribution function of the two-parameter model may be expressed as

$$P_f = 1 - \exp[-L(\sigma/\sigma_c)^w] \qquad (1)$$

where P_f is the probability of failure of a fibre of length, L, failing at a stress, σ, and w is the Weibull modulus. The measured values of the fibre strengths at each gauge length and treatment were ranked into ascending order and each value was assigned a

linearly distributed value of P_f between 0 and 1 according to

$$P_f(j) = \left(\frac{j - 0.5}{n}\right) \qquad (2)$$

where P_f is the probability of failure for the jth observation and n is the total number of test observations in the set.

Weibull plots of $\ln \ln 1/(1 - P_f)$ versus $\ln \sigma$ were constructed by a computer program and a linear regression was carried out to fit a straight line to the data. The gradient of this curve is the Weibull modulus, w, and the intercept yields the characteristic strength or scale parameter for that particular gauge length.

2.2.2. In-resin strength study
Micromechanical modelling of composite strength and interface behaviour must be based on reliable data for fibre strengths. It is not convenient to measure the strength of single fibres in air at gauge lengths below about 10 mm; the data are not reliable due to experimentally induced scatter and biomodality. This results in large errors in estimating the strength of short fibre segments (10–100 μm) which is a requirement of the micromechanics model. For this reason the strength of the fibre embedded in resin was estimated. A single fibre was embedded into a cast-resin test piece. This was then extended monotonically and the incidence of fibre fractures was monitored using a light microscope. The ultimate mean fragment length is used as the basis of the strength estimation.

Wagner and Eitan [3] and Yavin et al. [4] recently proposed that this test may be used to determine the strength of a fibre. They described the dependence of the average fragment length on the applied stress and they considered that, up to the saturation strain (after which no further fibre fractures can occur), the probability of interaction between breaks is extremely low. In this way the fragmentation test can be regarded as a "multiple tensile test" with a chain of samples, each being independent of the other samples and obeying the Weibull strength distribution. The mean tensile strength, $\bar{\sigma}$, of fibres of length L is given by

$$\bar{\sigma} = \sigma_c L^{-1/w} \Gamma\left[1 + \frac{1}{w}\right] \qquad (3)$$

where Γ is the gamma function.

The next step is to consider the fragmentation test as a tensile test in which independent samples of varying lengths are subjected to an applied stress. Equation 3 is then adopted in reverse form to give the average fragment length, L

$$\bar{L} = \sigma_c^w \sigma_t^{-w} \left[\Gamma\left(1 + \frac{1}{w}\right)\right]^w \qquad (4)$$

Data can be generated for a set of fragment lengths as a function of applied stress during a continuously monitored experiment. A plot of $\ln L$ versus $\ln \sigma_t$ should produce a straight line of gradient $-w$ and an

intercept equal to

$$w\left[\ln \sigma_c + \ln \Gamma\left(1 + \frac{1}{w}\right)\right] \qquad (5)$$

from which the characteristic strength, σ_c, may be obtained.

The ineffective length, μ, is that length over which the stress is transferred, and a shorter fibre fragment can, therefore, never break as it will never reach its failure stress. This will have an important effect on the results, particularly on the present work with untreated fibres, where the ineffective length is greater. It will also become more important as the test proceeds and the remaining amount of "available" fibre (that is, fragments of length greater than the ineffective length) is reduced. We have therefore incorporated a correction for the ineffective length so that Equation 4 becomes

$$(\bar{L} - \mu) = \sigma_c^w \sigma_t^{-w}\left[\Gamma\left(1 + \frac{1}{w}\right)\right]^w \qquad (6)$$

The correction factor is μ. We may then plot $\ln(L - \mu)$ versus $\ln \sigma_t$ to obtain w and σ_0.

2.2.3. Adsorption isotherm studies

X-ray photoelectron spectroscopy (XPS) is often used to characterize the surface of carbon fibres with respect to changes in surface composition. A straightforward analysis yields the atomic percentage of surface elements, principally C, N and O in the case of carbon fibres. Further information on the chemical state(s) of these elements may be obtained by peak fitting, which involves deconvoluting the C1s peak into components of different binding energies and associating these with particular oxygen-containing groups (for example, –OH, –COOH). A second method involves labelling specific surface sites by chemical "tags" which can be easily monitored by XPS. However, there are problems associated with both these methods, the first can only be used when there is a clear shift in the C1s peak, which is not always the case with commercial fibres, and the second method is usually only used to determine one data point with a saturated labelling solution and monitoring the uptake of the tag. The present method of creating adsorption isotherms was developed in order to overcome some of these difficulties and to obtain additional information on the nature of the bond formed with the adsorbed species.

50 mm lengths of tow of untreated fibres and those treated at 10, 25, 75, 100 and 400 C m^{-2} were soaked in solutions of magnesium sulphate in deionized water at increasing concentrations from $0.001S_0$ to S_0 (the saturated solution). Untreated fibres, and those treated at 25 and 100 C m^{-2} were also treated in solutions of silver nitrate from $0.0001S_0$ to S_0. The fibres were soaked for 30 min and then rinsed thoroughly, the untreated fibres in deionized water and the latter in pure ethanol (as water was found to leach off the adsorbed silver) and then all the fibres were dried in an oven at 60 °C. The fibres were then analysed by XPS and the atomic concentrations of Mg and S (or Ag and N (corresponding to the –NO$_3$ ion))

were determined. The S and –NO$_3$ data were used to correct the Mg and Ag concentrations, respectively, for any residual MgSO$_4$ or AgNO$_3$ which had not been rinsed from the surface. This gives a more accurate measure of the adsorbed ion (Mg or Ag). Up to eight data points were generated for each particular fibre-treatment level and adsorption experiment. The means of these data were then used to construct plots of the respective adsorbtion isotherms.

2.3. Interface adhesion studies
2.3.1. Fragmentation tests

The single-fibre fragmentation test was used to study the adhesion between the fibres and the epoxy resin. This test does not directly measure the bond strength but the experimental data may be analysed by the use of stress-transfer models. The measured distributions of fragment lengths were used as a sensitive indicator of changes at the interface. The Kelly/Tyson model, was then adopted to estimate an interfacial-shear strength. The validity of this procedure was explored in the light of recent results from other workers, and a correction factor was incorporated to allow for the strength/length dependency of the fibre.

The single-embedded-fibre-composite samples were tested on a straining stage attached to a light microscope. The samples were extended monotonically until no further fibre fractures were observed. The fragment lengths were measured using a vernier attached to the movable stage of the microscope. The distribution of these lengths relates to the effectiveness of the bond; a shorter fragment length indicates a more efficient bond. Six samples of each fibre type were tested and the results were grouped for analysis.

2.3.2. Pull-out tests

The second model test used to study the interface was the pull-out technique. A single fibre was partially embedded in a small cylinder of liquid resin contained in a brass holder. The resin was cured and the force needed to pull out the fibre was then measured. In this test, also, the complex stress distribution around the embedded fibre precluded simple data reduction. In the present work, two analyses, one based on a shear-strength criterion and one on a fracture-mechanics model were applied to study the resultant pull-out load/displacement traces. These analyses were compared and a new model which combines both principles is proposed. This appears to fit the experimental data reasonably well and it is considered to be more consistent with experimental reality. From the new model it was possible to generate information on the coefficient of friction and shrinkage stress at the interface as well as on the interfacial bond strength and fracture toughness.

The pull-out test used was based on an adaptation by Pitkethly and Doble [5] of the test developed by Desarmot and Sanchez at ONERA [6]. The fibre was embedded in resin in a holder and then the free length was guided into a hole in a fixture at the base of a soldering iron attached to the top grip of a tensile

testing machine. The top grip was lowered leaving 3 mm of fibre between the resin and the iron. The soldering iron was then turned on and solder applied. While the solder was molten, the load cell of the testing machine was zeroed. The iron was then switched off. The solder gripped the fibre, as it solidified, and the thermal contraction of the iron was then used to pull the fibre smoothly from the resin. The embedded length and fibre diameter were measured after the fibre had been pulled out of the resin by examination using scanning electron microscopy (SEM). Up to 48 fibre samples at each of the levels U, 10, 25, 50 and 100 were tested.

3. Results

3.1. Fibre strength

An example of a cumulative-distribution plot of P_f versus σ_f on linear axes for the fibres tested is shown in Fig. 1a and a sample Weibull plot is shown in Fig. 1b. In most cases bimodal behaviour was observed. However, the distribution appears to be unimodal in some cases, but it is only at levels 5, 25 and 400 that unimodal behaviour is observed at all gauge lengths. In these cases, a single straight line (of gradient w) can be fitted to the data, indicating a good fit to the Weibull model. The values of the Weibull modulus calculated from the slope of the lines fitted to the plots of ln ln $(1 - P_f)$ versus ln σ for the individual sets are given in Table I. These Weibull moduli are lower than might be expected due to the assumption of unimodal behaviour which is implicit in the model. The Weibull moduli are also expected to be similar at each gauge length for a single fibre type and treatment level but this is clearly not the case. The three values for each surface treatment have therefore been averaged to give a value for w which is used as a basis for comparison. These values are also given in Table I, as are the values of the length-dependent characterisitic strength calculated from the intercept of the straight line with the x-axis. These values show the expected length dependency, shorter lengths being stronger. There are peaks in strength at surface treatment levels 5 and 25. In Fig. 2 the ln $\bar{\sigma}$ (mean strength) versus ln L plots for all the sets of fibres are shown. It can be seen that there is a clear trend in the data, although there are considerable variations from batch to batch. In this type of plot the slope is $(-1/w)$. The Weibull moduli of the individual sets vary from approximately 4–12 with the underlying trend being about 7.3. This is higher than the averages for the individual sets, as is often observed when a comparison is made between the two types of Weibull plot.

3.2. Fibre strength in resin

Typical plots of ln $(L - \mu)$ versus ln σ are shown in Fig. 3a and b and they are linear. Fig. 3c shows the comparison with fibres tested in air. This is a similar plot to that of Fig. 2 but the length scale has been extended so that the in-air and in-resin data can be plotted on the same graph. The group of lines to the right are the same as in Fig. 2. On the left are the plots
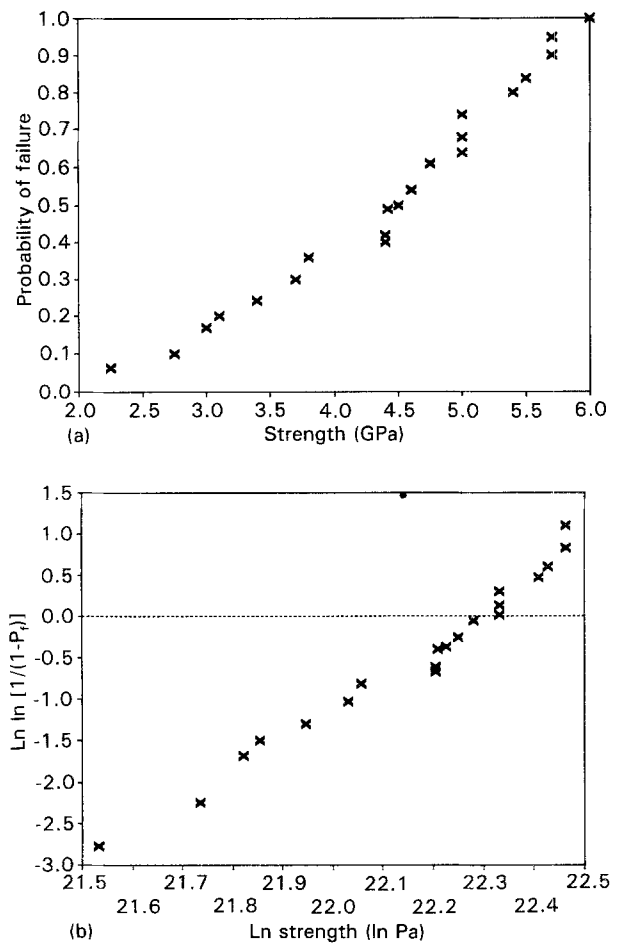

Figure 1 (a) A cumulative-distribution plot, on linear axes, of fibre strength versus the probability of failure for a typical set of single-carbon-fibre tensile tests conducted in air. (b) A cumulative distribution plotted on Weibull axes of ln ln$[1/(1 - P_f)]$ versus ln(strength). This set shows a unimodal distribution.

TABLE I Tensile strength of single carbon fibres tested in air

Surface treatment level (C m^{-2})	Weibull modulus (w)				Characteristic strength, σ_c (GPa)		
	Gauge length (mm)			Mean	Gauge length (mm)		
	12	30	75		12	30	75
0	3.4	4.4	3.5	3.8	5.0	4.6	3.6
1	3.6	3.7	4.3	3.9	4.7	4.6	3.6
3	4.8	3.9	4.7	3.8	4.7	4.2	3.9
5	3.4	3.7	5.2	4.1	5.0	4.7	4.3
10	4.3	3.7	3.7	3.9	5.1	4.0	3.8
15	3.7	4.8	4.1	4.2	4.3	4.0	3.3
25	4.8	3.9	3.8	4.2	5.2	4.5	3.8
50	3.5	3.7	4.7	4.0	4.7	4.5	3.6
75	4.1	4.7	3.8	4.2	4.7	3.9	3.6
100	4.6	4.5	4.7	4.6	4.9	3.9	3.6
400	3.6	2.9	2.9	3.1	4.8	4.1	3.8

derived from the in-resin tests. The strength-to-length trends are similar but the in-resin strength is significantly less than that in air at comparable gauge lengths. The Weibull shape parameters are similar. Values of the Weibull scale parameters for a unit length of 1 mm have been calculated from the data
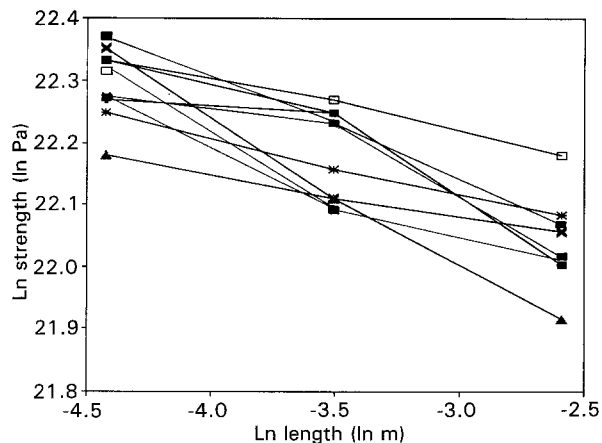
Figure 2 Plots of ln $\bar{\sigma}$ versus ln L for all sets of tensile tests on single carbon fibres in free air.

in Table I, using the weak-link scaling method (Equation 7), and they are given in Table II.

$$\sigma_1 = \sigma_2 \left(\frac{L_2}{L_1}\right)^{1/w} \tag{7}$$

The strengths of lengths equal to the gauge lengths used in the single-fibre study, 75 mm, 30 mm and 12 mm were been calculated. Characteristic-strength or scale-parameter data show exactly the same trends as for the single fibres, peaking at level 5 and level 25 with a further slight rise at level 100. The range of strength is greater and it seems that the effect of the resin is to exaggerate this behaviour. These strengths are all much lower than their counterparts determined in free air, as shown in Fig. 3c. This is possibly due to the fact that the weak-link scaling procedure may not be appropriate to this material. However, as the determined strengths are for 1 mm, and the fragment lengths are close to this, it should be possible to obtain a reasonable estimate of the fragment strength. This was carried out and the results are given in Table II. One problem which has not been addressed, is that the strain in the resin might not be equal to that in the fibre. Figueroa *et al.* [7] have recently proposed that there is in fact a lag. This possibility has been disregarded in the present work.

3.3. Adsorption isotherms

Isotherms for fibres treated at level 25 for both Mg and Ag are shown in Fig. 4. They show typical chemisorption behaviour with an initial sharp increase followed by a plateau. There is considerable scatter in the data, but this is to be expected due to the variability of the treatment along and within the tow. The data show a reasonable fit to a Langmuir model and the parameters thus obtained have been used to construct the curves shown in Fig. 4. Values for mono-layer coverage (x_m) are then calculated from the initial slope of the lines for each fibre type for both magnesium and silver adsorbtion. However, before any acidity values may be calculated, it is necessary to consider the number of –COOH groups which would bond to each labelling ion. This will be discussed later.
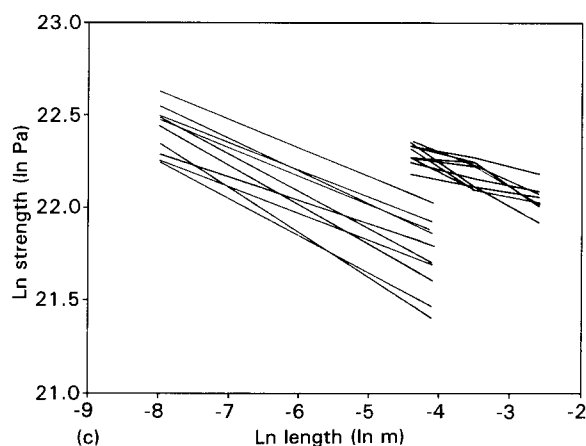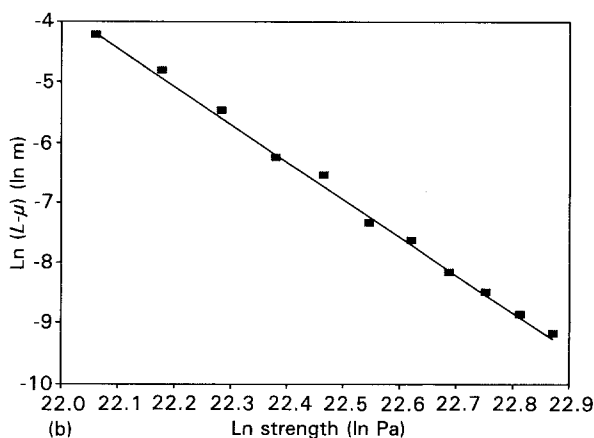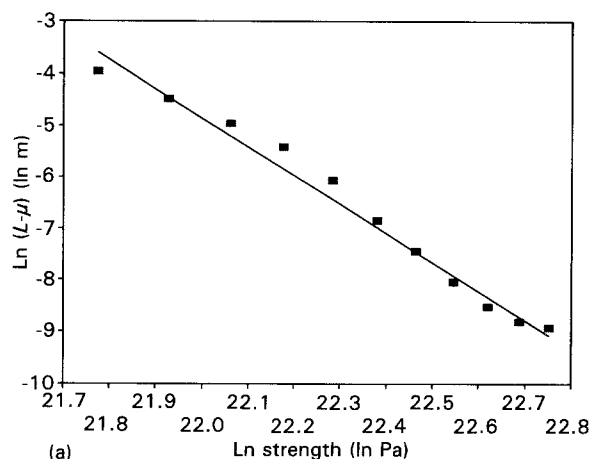

Figure 3 (a) Plot of $\ln(L - \mu)$ versus $\ln \sigma$ for embedded fibres with surface treatment of (a) 5 C m^{-2} and (b) 25 C m^{-2}. The stress, σ, is derived from the measured strain at the relevant fragment length. (c) A global plot of ln σ versus ln L for both the embedded-fibre tests and the tests in free air. The embedded data has been transferred from plots of the type shown in (a) and (b). These are to the lower left. The data for the tests in air is the same as Fig. 2, with the axes suitably adjusted. These plots are the group at the upper right.

3.4. Fragmentation tests

Cumulative distributions were plotted for the measured fragment lengths for each of the fibre types tested and these are shown in Fig. 5, all on the same axes. They show a progressive shift to the left, to shorter fragment lengths, with increased treatment level. The median value of these data is plotted against the surface-treatment level in Fig. 6. This shows a sharp initial fall in fragment length but then a levelling out

TABLE II Strength of single carbon fibres embedded in epoxy resin

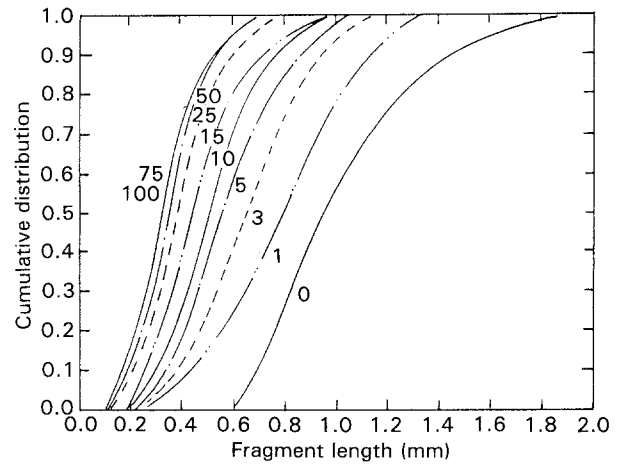| Surface treatment level (C m^{-2})	Weibull modulus (w)	Characteristic strength, σ_c (GPa) at gauge length (mm)			
		1 mm	12 mm	30 mm	75 mm
0	4.0	4.2	2.3	1.8	1.4
1	6.8	4.4	3.0	2.3	2.3
3	6.1	5.5	3.7	3.2	2.7
5	5.6	6.0	3.8	3.3	2.8
10	6.7	5.0	3.4	3.0	2.6
15	4.8	5.4	3.2	2.6	2.2
25	6.3	6.4	4.3	3.7	3.2
50	4.9	4.5	2.7	2.2	1.9
75	7.8	4.4	3.2	2.8	2.5
100	4.7	5.1	3.0	2.5	2.0

Figure 5 Cumulative distributions of the saturation fragment lengths for all the embedded fibres tested.
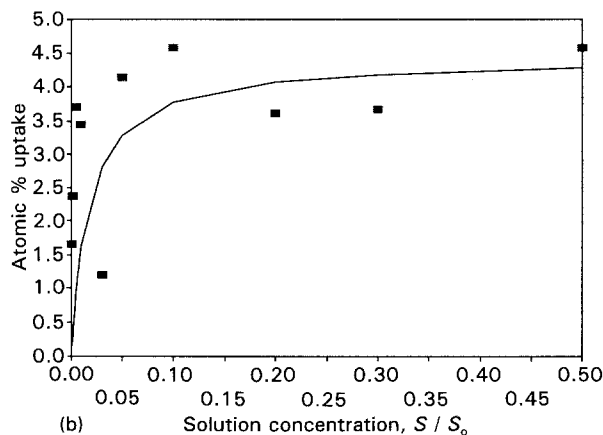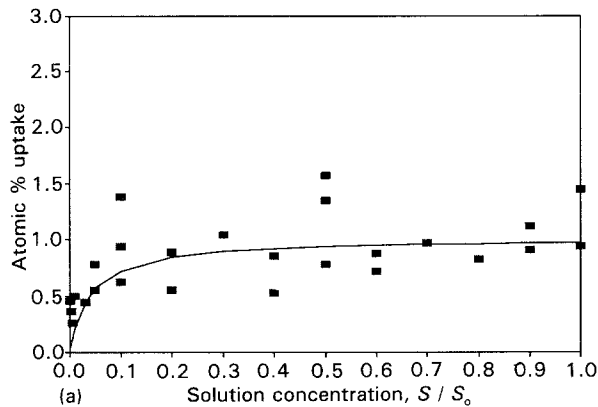

(a)

(b)

Figure 4 Adsorption isotherms for the uptake of (a) magnesium and (b) silver from solution onto fibres treated at the 25 level, showing the calculated fit to Langmuir isotherms.

Figure 6 Median fragment length, $\bar{L}$, versus surface-treatment level derived from the embedded-single-fibre fragmentation tests.

above the 25 treatment level at about 0.3 mm. The median values for each treatment level are given in Table III.

The distribution of fragment lengths has been used by many workers to calculate the interfacial shear strength using the Kelly–Tyson model [9]. In order to estimate the critical length it is assumed [8] that the measured lengths must lie between L_c and $L_c/2$ and that $\bar{L} = 3L_c/4$. This, however, assumes a unique fibre strength; whereas, in fact, the strength of the fibre is length dependent, so that as the fragments get shorter
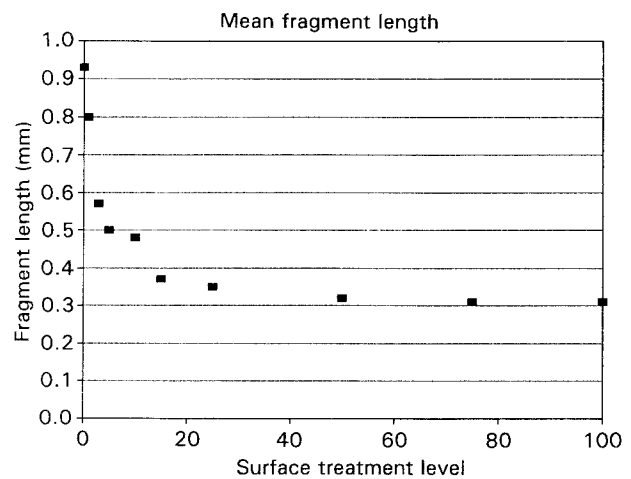
a higher stress is required to initiate subsequent breaks. Henstenburg and Phoenix [10] and Netravali et al. [11] have developed a Monte-Carlo simulation to estimate fragment strength. It is based on the Poisson–Weibull model for fibre strength. The mechanical model for stress transfer is that of Kelly and Tyson, which assumes a constant interfacial-shear stress in the shear-transfer zone. This assumption is used for simplicity since it captures the essential nature of the stress distribution, it also has the benefit of avoiding subjective, non-linear-curve-fitting routines, or other numerical methods to estimate the shear strength. The mean fragment lengths are used to calculate a correction factor which can be inserted into the Kelly–Tyson model as follows, for calculation of the interfacial shear strength

$$\tau_i = \frac{d_f \sigma_c}{2\bar{L}}\left(\frac{\bar{\Lambda}_w}{2}\right)^{(w+1)/w} \tag{8}$$

where d_f is the fibre diameter, σ_c is the characteristic strength or Weibull scale parameter at the average fragment length $\bar{L}$ and $(\bar{\Lambda}_w/2)^{(w+1)/w}$ is the correction factor. The parameter $\bar{\Lambda}_w$ is a dimensionless estimated

TABLE III Data from embedded-carbon-fibre fragmentation tests

Surface treatment level $(C\,m^{-2})$	Mean ultimate fragment length, $\bar{L}$ (mm)	Correction factor (see Equation 8)	Mean fibre diameter (μm)	Fragment strength (GPa)	Interfacial shear strength, τ_i (GPa)	L_{max}/L_{min}
0	0.93	0.90	6.80	4.3	14.0	3.0
1	0.80	0.82	6.80	5.0	15.7	3.0
3	0.57	0.86	6.80	6.0	30.8	4.0
5	0.50	0.86	6.85	6.8	40.0	3.0
10	0.48	0.82	6.85	5.5	32.2	3.0
15	0.37	0.87	7.00	6.0	54.3	3.0
25	0.35	0.83	6.90	7.6	62.2	4.0
50	0.32	0.87	6.76	5.7	52.4	3.5
75	0.31	0.81	6.96	5.1	46.3	4.0
100	0.31	0.87	7.07	6.6	65.5	3.5

mean fragment length derived from the Monte-Carlo simulation and w is the Weibull modulus.

Calculated values of this correction factor are given in Table III. They are about 15% higher than the factor 3/4 which has been used in the past, and they make a significant difference to the results. Henstenburg and Phoenix mention that tensile tests on single fibres are required to generate the necessary strength data, but in the present case the in-resin strength parameters from Table III have been used. The values of the interfacial shear strength, τ_i, are also given in Table III.

3.5. Pull-out tests
3.5.1. Introduction
In order to understand the pull-out process and to produce an analytical model which is physically plausible, it is necessary to consider the actual mechanism of debonding and its effect on the stress profiles in the fibre and at the interface.

In the pull-out test, the fibre is pulled from a small cylinder of resin by traction applied to the free end. A quasi-constant displacement rate, in the axial direction is maintained. The load–displacement traces vary according to the depth embedded and other experimental and material variables. Examples of the traces observed are shown in Fig. 7, and a number of characteristic loads, P^*, P_0 and P_f are indicated. In Fig. 8, some examples are shown of the relationship between embedded length and maximum debond stress, σ^* (derived from P^*). Schematic diagrams of the test configuration, showing the tensile-stress distribution in the fibre and the shear stress at the interface as the fibre is loaded and then as it debonds progressively from the point of entry, are shown in Fig. 9.

On loading, stress is transferred from the fibre to the surrounding matrix by shear at the fibre–matrix interface. The resultant load–displacement curves given in Fig. 7 show an initial linear region corresponding to elastic loading of the fibre with a bonded interface. The stress profiles are indicated in Fig. 9a for the tensile stress in the fibre and the shear stress at the interface. These will follow a typical Cox type distribution [12] the maximum value being found close to the point of entry of the fibre. In reality the shear stress
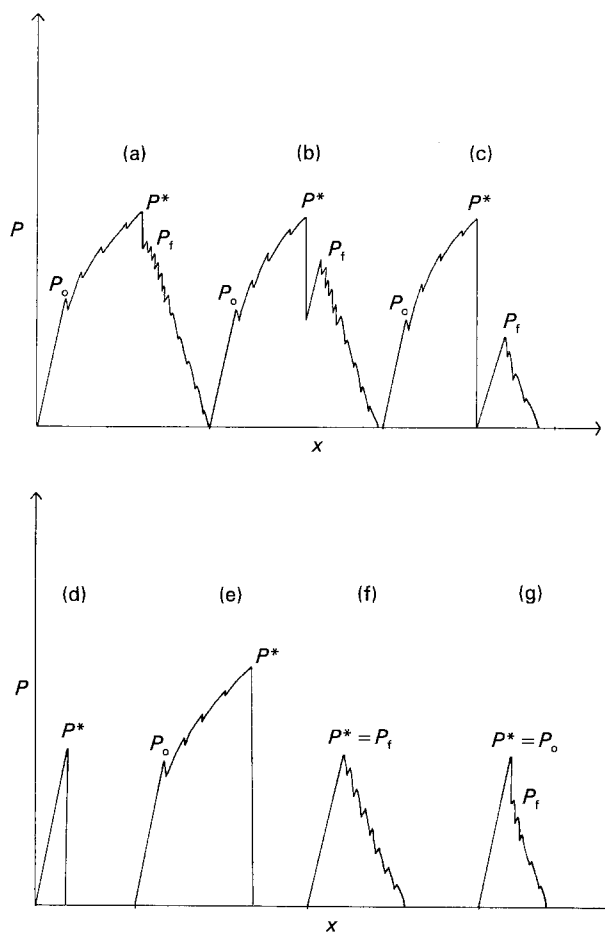

Figure 7 Notional load–displacement curves for pull-out tests, illustrating: (a) stable debonding and pull-out, (b) partially stable 1, (c) partially stable 2, (d) unstable debonding and pull-out, (e) unstable pull-out, (f) no bonding, and (g) no friction during debonding.

must be zero at the free surface; however, the maximum is so close to the surface that it acts as a stress concentration and initial debonding occurs at a force P_0, the frictionless debond load, in Fig. 7a. The debond-crack may then propagate in either a stable, or in an unstable manner, depending on the conditions of testing. If the machine loading system is insufficiently hard then the fibre will debond and pull-out catastrophically. This is shown in Fig. 7d and this may
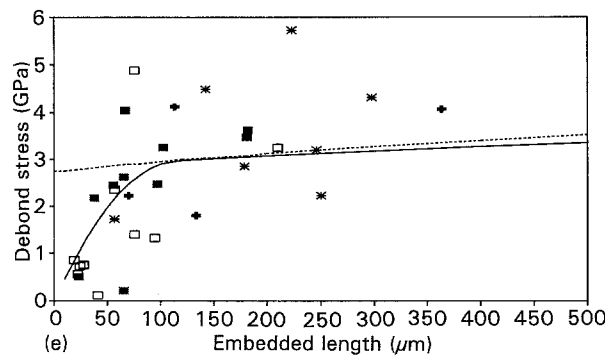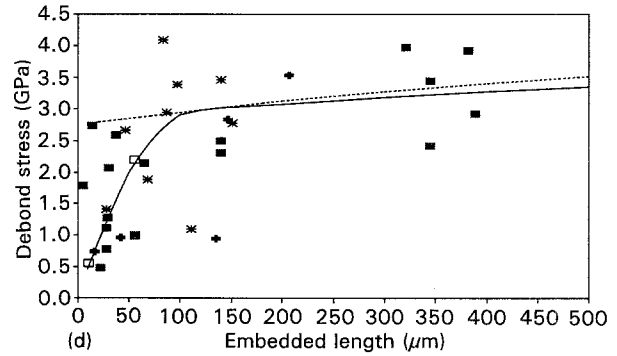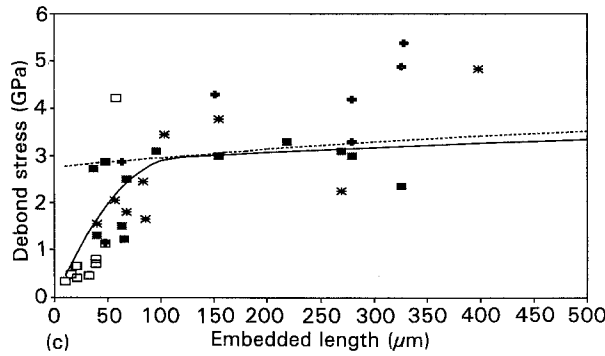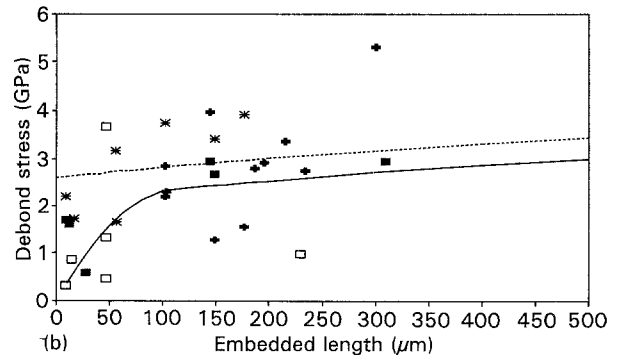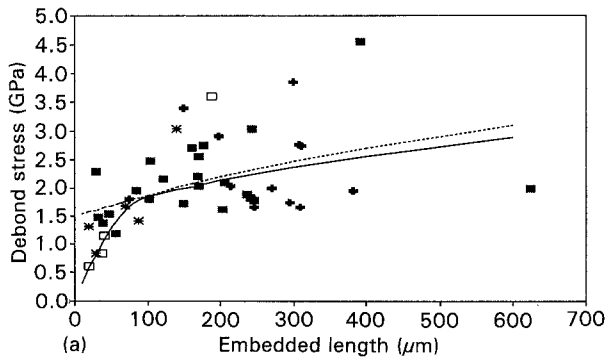
Figure 8 The maximum debond stress, σ_0, versus embedded length plots for pull-out tests on fibres treated to levels (a) 0, (b) 10, (c) 25, (d) 50 and (e) 100 C m^{-2}. The data has been grouped into stability categories, and plots showing the predictions of the models of (———) Gao *et al.* and (——) Hsueh are also displayed. (■) Stable, (+) partially stable 1, (*) partially stable 2, (□) unstable.

also occur if the fibre is below a critical length, which we will call z_{max}.

If the crack propagates in a stable manner to the stage shown in Fig. 9b then stress is also transferred by friction at the debonded interface. This frictional force arises from a radial compressive stress, q_0, in the resin due to differential shrinkage or contraction during cooling from the fabrication temperature, since the thermal-expansion coefficient of the matrix is higher than that of the fibre. This stress is not uniform along the length of the fibre due to transverse (Poisson's) contraction of the fibre in the radial direction when it is subjected to an axial tensile stress. There will be complementary displacement in the resin which will alter the radial pressure exerted on the fibre. A schematic stress distribution is given in Fig. 9b and it shows the stress profiles in the bonded, z and debonded $L - z$, regions. In the debonded region the stress profile is shown to be linear. In fact, due to Poisson's ratio, it will be slightly curved. Further increases in the applied load will simply displace the debonded zone. This is demonstrated by the rising portion of the pull-out-load–displacement plot from P_0 to P^* given in Fig. 7a.

At the point where the length of the bonded region has decreased to the critical length, that is, when the crack length has reached z_{max}, shown in Fig. 9c, the remainder of the fibre will debond in an unstable manner and the fibre will start to pull-out of the matrix. This instability is represented by the stress profile given in Fig. 9c where it can be seen that there is an insufficient remaining length of fibre for the stress to be transferred in a stable manner. This is indicated on the load–displacement plot by a drop from P^*, the maximum debond load, to P_f, the frictional pull-out load, as shown in Fig. 7a. An additional contribution to the pull-out process is the relaxation of the strain in the fibre as the tensile stress falls following debonding.

On debonding, the load may fall to P_f (Fig. 7a), or it may fall below P_f and then rise again (Fig. 7b), or it may drop to zero followed by a rise (Fig. 7c). It may also fall to zero and remain there (Fig. 7d and e). This will to a certain extent depend on the testing system. As mentioned above, if the system is insufficiently hard or the embedded length is below z_{max} then the load will stay at zero (Fig. 7b and c). However, for all other cases the drop will be arrested by the radial expansion of the fibre, due to the relaxation of Poisson's contraction at P_f. The fibre will then continue to pull-out with frictional drag, shown by the falling stick–slip portion of the load–displacement plot in Fig. 7a, c, d and e. The corresponding stress profile is given in Fig. 9d.
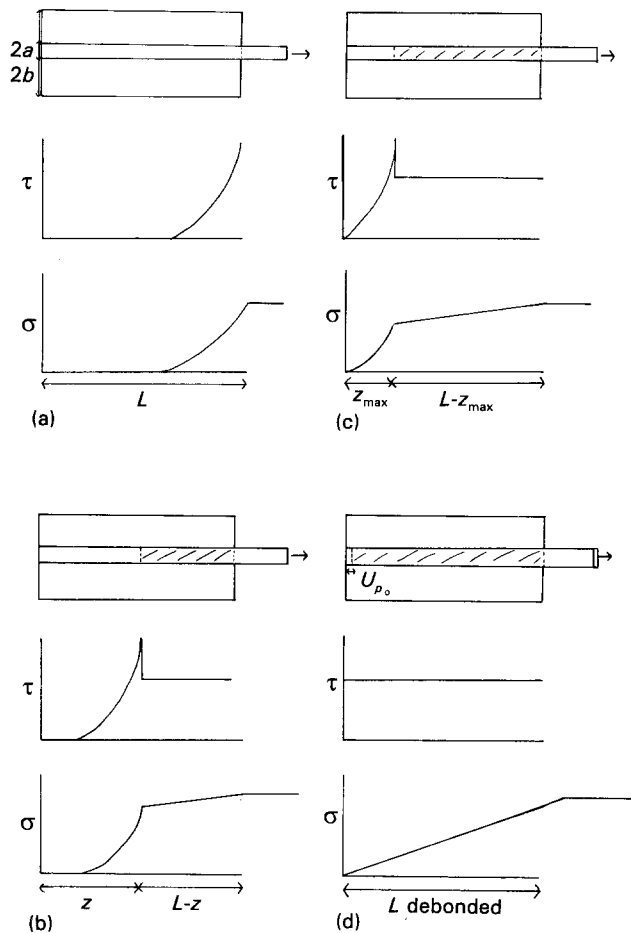
Figure 9 Schematic diagrams of axial stress, σ and shear stress, τ, distributions in bonded and partially debonded fibres in resin in the pull-out test: (a) interface still bonded, (b) debonding to z, (c) debonding to z_{max}, and (d) fibre totally debonded.

If P_f is equal to P^*, as shown in Fig. 7f, then the debonding event is always stable. This is usually only the case with ceramic composites where there is no chemical bonding at the interface. A further situation may occur if the compressive stress, q_0, is very low and is completely relieved by radial Poisson's shrinkage of the fibre. In this case P_0 will be equal to P^*, as shown in Fig. 7g.

If we consider that the free length in the present experimental work is ~ 1 mm, it is evident that the elastic strain energy relaxation effect, as the fibre is unloaded, will be significant. As a result of the axial relaxation at debond, the fibre will instantaneously pull-out in an unstable manner by an amount U_{po} shown in Fig. 9d.

A value of U_{po} has been estimated by the development of an approximate model based on force-balance principles. It assumes that stress transfer in the bonded and debonded portions of the embedded length is linear (Kelly–Tyson model) with constant, but different, interfacial-shear strengths along each zone. Using values from the present experimental work, a value for U_{po} of 11 μm was estimated. This is significant, as it is of the same order as the shortest embedded lengths and could be an additional factor contributing to the unstable pull-out at very short embedded lengths.

In the analyses which follow, the following numerical values have been assumed: $E_f = 230$ GPa, $E_m = 3.0$ GPa, $\nu_f = 0.2$, $\nu_m = 0.4$, $a = 0.003$ mm, and $b = 1.0$ mm.

3.5.2. Gao–Mai–Cotterell model

This fracture-mechanics-based model considers the debonding process as crack propagation at the interface. The standard models [13, 14] do not include the effects of friction and Poisson's contraction. The model by Gao et al. [15] considers both. Crack initiation is not included in the model and it assumes a pre-existing debond of length $(L - z)$.

During the debonding process, for systems where $b^2 > a^2$, the instantaneous or partial debond stress, σ_d^p, is given as a function of the debond length, $(L - z)$ by

$$\sigma_d^p \approx \sigma_0 + (\bar{\sigma}) - \sigma_0[1 - \exp(-\lambda(L - z))] \qquad (9)$$

where λ is equal to $2\mu k/a$, μ being the coefficient of friction at the interface and $k = (\alpha\nu_f + \gamma\nu_m)/\{\alpha(1 - \nu_f) + 1 + \nu_m + 2\gamma\}$. $\alpha = E_m/E_f$ (Young's modulus ratio for the matrix to the fibre), $\gamma = a^2/(b^2 - a^2)$ and ν_m and ν_f are the matrix and fibre Poisson ratios respectively. λ may be determined experimentally.

The asymptotic debond stress, $\bar{\sigma}$, which is reached at a long embedded length L is given by

$$\bar{\sigma} = -\left(\frac{q_0}{k}\right)\left[1 + \left(\frac{\gamma}{\alpha}\right)\left(\frac{\nu_m}{\nu_f}\right)\right] \qquad (10)$$

where q_0 is the clamping stress. $\bar{\sigma}$ can be determined experimentally from the total debond load/embedded length plot shown in Fig. 8.

The frictionless debond stress, σ_0, is defined in terms of the interfacial fracture toughness, G_{ic}, as

$$\sigma_0 = \left\{\frac{4E_f G_{ic}[(1 - 2k\nu_f) + (\gamma/\alpha)(1 - 2k\nu_m)]}{a(1 - 2k\nu_f)^2}\right\}^{1/2}$$

$$\approx \left[\frac{4E_f G_{ic}}{a(1 - 2k\nu_f)}\right]^{1/2} \qquad (11)$$

P_0, which is equal to $\pi r^2 \sigma_0$, is indicated in Fig. 7 and is taken in this model to be a constant value, regardless of the embedded length. The stress profile depicted by this model does not therefore consider the stress transfer in the bonded zone in Fig. 9.

The immediate advantage of the model of Gao et al. is that it is possible to test against experimental data since the three parameters, σ_0, λ and $\bar{\sigma}$ can be determined directly.

A systematic study was made of the type of trace and the value of the debond and frictional stresses in relation to the associated embedded length. Four main types of trace were observed. The first will be referred to here as *stable debonding* and it corresponds to Fig. 7a, although the initial-debond-stress features were observed only occasionally. A second type will be labelled *partially stable 1* and it is shown in Fig. 7b. The third type is represented by Fig. 7c and it is referred to as *partially stable 2*. The final type is *unstable* and is represented by Fig. 7d and e. The

maximum debond stress versus embedded length plots are then classified by trace type, and it can be seen in Fig. 8 that, if we consider only the stable debonding, the scatter is much reduced.

From the parameters determined in the above analysis, the maximum debond stress for the model of Gao et al., was calculated from Equation 9 and plotted versus the embedded length in Fig. 6 for all fibre types. A reasonable fit to the *stable* data is observed at long lengths but there is a departure from the Gao model at low embedded lengths. The values of the fracture energy, G_{ic}, are given in Table IV and show an increase in the interface fracture toughness up to treatment-level 25.

3.5.3. The Hsueh model

If the Hsueh model [16, 17], which is based on a shear-strength criterion, is expressed in a similar form to the model of Gao et al., it is easier to compare the two models directly. Therefore, the relevant equations have been rearranged by Kim et al. [18, 19] and are shown here in the new format. The pull-out process is described in exactly the same way as before but without the assumption of an initial crack. In this case the partial-debond stress for $b^2 \gg a^2$ is given by

$$\approx \sigma_0 + (\bar{\sigma} - \sigma_0)\left[1 - \frac{B_1}{(\lambda + B_2)}\right] \quad (12)$$

where σ_0 is determined from the analytical solution for the fibre stress at the free matrix surface when the interfacial-shear stress equals the shear bond strength, τ_b

$$\sigma_0 = \left[\frac{2\tau_b(1 + \gamma/\alpha)}{\beta a}\right]\tanh(\beta L) \quad (13)$$

$$\beta = \left\{\frac{1 + \alpha/\gamma}{(1 + v_m)[b^2 \ln(b/a) - (a^2/2\gamma)]}\right\}^{1/2} \quad (14)$$

The parameters B_1 and B_2 are a function of the partial debond length, $L - z$

$$B_1 = \frac{(m_1 - m_2)\exp[(m_1 + m_2)(L - z)]}{\exp[(m_1(L - z)] - \exp[(m_2(L - z)]} \quad (15)$$

$$B_2 = \frac{m_1\exp[(m_1(L - z)] - m_2\exp[m_2(L - z)]}{\exp[(m_1(L - z)] - \exp[(m_2(L - z)]} \quad (16)$$

where $m_1 = -[\Omega + (\Omega^2 - 4\Omega\lambda)^{1/2}]/2$ and $m_2 = -[\Omega - (\Omega^2 - 4\Omega\lambda)^{1/2}]/2$ and $\Omega = -(\beta^2/\lambda) \times \{[1 + (\alpha/\gamma)(v_f/v_m)]/[1 + (\alpha/\gamma)]\}$ which can be simplified to $\Omega \approx -(\beta^2/\lambda)(v_f/v_m)$ for $b^2 \gg a^2$.

The two theories discussed above are similar in that the partial-debond stress, σ_d^p, is composed of two components: a frictionless-debond-stress component and a friction-stress component. This latter stress is directly proportional to $(\bar{\sigma} - \sigma_0)$ and is controlled by λ (which is related to the coefficient of friction). The major difference between the two models is in the form of the frictionless debond stress, σ_0. In the model of Gao et al., σ_0 is independent of the embedded length and is described by a fracture energy G_{ic}. Hsueh uses a shear strength to describe σ_0 which is dependent on the embedded length, approaching a constant value only at longer lengths.

The next step was to see if the data could be fitted using the Hsueh model. As there is no easy way to determine specific parameters from a fit to this model without a complicated non-linear fitting routine, the values calculated above for λ and q_0 from the model of Gao et al. were used, as they should be virtually identical. However, a value for σ_0 could not be used as this has a completely different origin. In fact, it can be seen from Equation 13 that knowledge of the interfacial-shear strength is required. An average value for the shear bond strength, τ_b, can be determined from the initial gradient of the experimental maximum debond stress versus embedded length curve as [18]

$$\left(\frac{d\sigma^*}{dL}\right)_{L=0} = \frac{2\tau_b[1 + (\gamma/\alpha)]}{a} \quad (17)$$

These values have been determined for the present results and are given in Table IV. They show an increase up to level 25 with no further change after that. It was not possible to verify how well the Hsueh model fitted the data other than by calculating the complete function for the maximum debond stress versus embedded length and comparing this to the experimental values. This is not, however, as straightforward as with the Gao model, since the maximum debond stress is not necessarily the same as the complete debond stress in this case. In fact the embedded length, z_{max}, at which the maximum debond stress does occur, marks the transition between stable and unstable debonding. This is described more fully in papers by Kim et al. [18, 19].

Once values of z_{max} have been calculated, the Hsueh model can be used to determine a maximum debond stress versus embedded length plot to compare with experimental data. We first consider the maximum debond stress at embedded lengths $L > z_{max}$. Stable debonding proceeds until the debond length reaches $L - z_{max}$ and so the maximum debond stress will be

TABLE IV Parameters of the Gao–Mai–Cotterell model derived from the pull-out tests

Surface treatment level (C m⁻²)	Debond stress, σ_0 calculated (GPa)	Debond stress, σ_0 measured (GPa)	Debond shear stress, τ_b (MPa)	Friction shear stress, τ_f (MPa)	τ_b/τ_f	Debond fracture energy, G_{ic} (Jm⁻²)
0	1.50	1.77	43	12.2	3.5	7.3
10	2.60	3.50	53	12.2	4.3	22.0
25	2.76	3.90	66	12.2	5.4	24.8
50	2.74	3.50	66	12.2	5.4	24.5
100	2.74	3.50	66	12.2	5.4	24.8

calculated by substitution of z_{max} for z in Equation 12. This will be represented theoretically by a load–displacement plot, as in Fig. 7b, showing *stick–slip behaviour* on the rising curve.

If, however, the embedded length is less than z_{max}, the process is completely unstable, and the initial debond leads to complete debonding ($\sigma_0 = \sigma^*$). The load–displacement plot is as shown in Fig. 7b. When the embedded length is less than z_{max}, the frictional-stress component does not contribute to the maximum debond stress. Therefore the maximum debond stress is given by Equation 13, which is based on the assumption of unstable debonding [20].

The maximum debond stress was calculated in the above way using the parameters determined from the Gao et al. model and it is shown in Fig. 8 with the predictions of this latter model and the experimental data. Generally, the Hsueh model fits the data better at low embedded lengths. Below z_{max}, the model of Gao et al. overestimates σ^* because it is based on stable debonding and assumes a constant value of σ_0, rather than an increase with length. Above z_{max}, the Hsueh model slightly underestimates the maximum debond stress. We can see that the models give the best fit for the data which is designated *stable* in this study. This may be expected, since this assumption is the basis of both analyses. The calculated parameters generated from the above procedure are given in Table V.

3.5.4. Study of surface morphology

Fibres treated at level 25 were pulled out of the control resin in opposite directions compared with the fibre-processing direction. The resultant load–displacement traces were analysed in the same way as the previous data. Values of the frictional stress and the maximum debond stress were calculated, and the former was plotted against the embedded length for each fibre direction. The data fell into two distinct sets (Fig. 10), one direction having a higher frictional stress than the other.

The calculated values of the coefficient of friction are indicated in Table V and they show that when the fibre is pulled out in one direction there is more
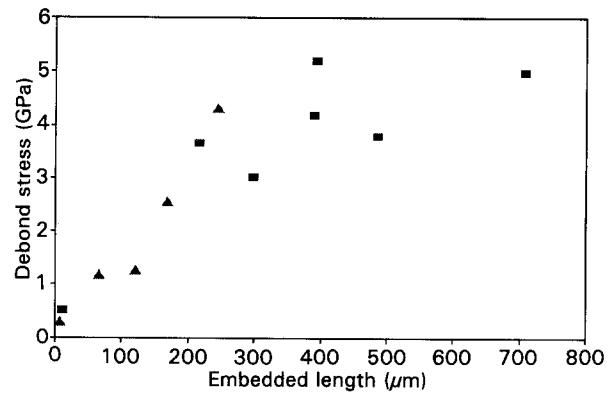

Figure 10 Friction-shear-stress component, τ_f, of pull-out as a function of embedded length showing directions (■) 1 and (▲) 2 of pull-out.

frictional drag than if it is pulled out in the other orientation. This reinforces the experimental evidence of Marshall and Price [21] and Klinklin and Guigon [22] which showed that graphite planes protruded from the surface at an angle. It is also an explanation for much of the scatter found in the pull-out data, as the original experiments were carried out with no regard to the embedding direction.

4. Discussion
4.1. Fibre strength

The mean fibre strengths in Table I show variations of the order of 20% over the range of surface treatments at each of the three gauge lengths. The data show considerable scatter, as evinced by the Weibull moduli in the range 2.9–5.2, and this makes it difficult to draw firm conclusions. Nevertheless, there appears to be a cyclic variation in strength with the surface treatment, with peaks at about level 5 and level 25. The high scatter may be attributed to the fact that too small a sample was tested and to batch-to-batch variability in the surface treatment. It should be noted, however, that all the fibre originated on a single spool and that the ln(mean strength) versus ln(length) plot (Fig. 2) shows a higher underlying Weibull modulus of 7.3. The strength variation with surface treatment is consistent with proposals [1, 23] of the removal of loosely adherent or flawed surface layers from the fibre for example. The cyclic behaviour may be attributed to removal of a layer, followed by etching of the more pristine layer thus exposed, and finally by removal of a second layer, the whole process then being repeated. It is very probable that the "true" treatment level varies from fibre to fibre in the tow due to screening of the fibres in the middle of the tow during the process of electrolysis. This means that experiments involving single fibres will be subject to more scatter than experiments using the whole tow. The tensile, fragmentation and pull-out tests fall in the former category whilst the XPS and adsorption involve the whole tow.

The observations of unimodal and bimodal Weibull distribution curves are more difficult to explain. The most plausable reason is that there were insufficient tests to establish the true pattern.

TABLE V Parameters of the Hseuh model derived from the pull-out tests

Surface treatment level (C m⁻²)	Hseuh friction parameter λ (m⁻¹)	Coefficient of friction, μ	Shrinkage stress, q_0 (MPa)	Debond stress $\bar{\sigma}$ (GPa)
0	1535	1.25	7.77 (10.2)[a]	4.2 (5.5)[a]
10	1530	1.25		
25	1349 (direction 1)	1.12		
	3387 (direction 2)	2.80		
	1514	1.25		
50	1425	1.25		
100	1587	1.25		

[a] Tested in a resin with a higher post-cure temperature.

4.2. Adsorption isotherms

In order to interpret the monolayer coverage of the labelling ion in terms of acidity, the number of acidic groups which react with each ion must be considered. Magnesium is known to form complex compounds with ligands which may be any monoatomic or polyatomic negative ion or neutral molecule. These latter always have one or more pairs of unshared electrons and are usually oriented so that one unshared pair points at the metal ion. Magnesium forms the most stable complexes with fluoride ions or oxygen as the donor. Even more stable is the chelating ligand which contains two or more functional groups so arranged that it can simultaneously occupy positions in the first co-ordination sphere of the same metal ion. If it is possible for the carbon fibre to act as a chelating ligand by providing several acidic groups to bond to the magnesium then the ion will be at its most stable. In the case of the surface of the carbon fibre it is likely that the flaws and pores where the acidity is thought to be positioned could provide more than one site and perhaps up to four if the geometry allowed for this. Magnesium is ideally surrounded by six ligands and so would accept other donor ions, probably OH^- from the water or the fibre surface, to fill up the remaining available positions. If we assume that four bonds attach to $-COOH$ in the standard case for the magnesium isotherms and assume a single valency for the silver, and assume that all the acidity is due to $-COOH$, then the acidity of the surface may be estimated using the method of Denison et al. [25].

Denison et al. took the volume for analysis to be that of a model surface segment of graphite, 10 nm by 10 nm by a depth of 3.5 nm. This latter is calculated from the inelastic mean free path for C1s photoelectrons with a kinetic energy of 1200 eV. Graphitic structure is assumed to exist up to 10 nm below the surface. The intensity of photoemission from atomic layers below the surface plane decays exponentially with depth according to the Beer–Lambert law. Integration of this function gives an analysis depth up to approximately 3.5 nm. From the density of graphite, Denison et al. then calculated the number of carbon atoms in this segment to be 40 000.

From the ratio of carbon to magnesium or silver for a monolayer covering of ions on the surface, the number of ions on a segment can be calculated. Acidic group density (number-of-acid-groups/carbon-content) is determined on the basis of the Mg bonded to four and the Ag bonded to one $-COOH$ group. If G is the geometrical area of the fibre calculated from the fibre diameter of 7 μm and density of 1.8 g cm^{-1}, R is a surface roughness factor of arbitrary value, usually taken to be 1.5, a is the number of acidic groups per surface segment and A is Avogadro's constant, then the surface acidity in units of μequivalents per gram is given by

$$\text{Acidity} = \frac{aGR \times 10^{22}}{A} \qquad (18)$$

The effect of the separation of COOH groups on uptake of magnesium is not taken into account here.

This would involve knowledge of the surface topography of the fibre tows. Calculated values of the number of acidic groups are presented in Table VI, and a rise in the level of acidity up to level 25 followed by a levelling is observed. Further details of this technique have been given by Baillie et al. [26].

4.3. Fragmentation tests

The strength data for fibres in-resin show similar trends to those of similar surface treated fibres tested in free air. This substantiates the argument for a cyclic variation in strength on to surface treatment due to removal of layer(s) from the fibre surface. It is proposed that the observed changes in the interfacial-shear strength may also be partly explained on this basis. For the untreated fibre the interfacial-shear strength is low due to low surface functionality, poor wetting and the presence of a loosely adherent surface layer. A small amount of treatment (5–10 C m^{-2}) leads to an increased shear strength, mainly due to removal of the surface layer. On subsequent treatment, increased surface functionality contributes to a further increase in the shear strength, but this peaks at about level 25 with the present fibre, probably because the shear strength of the interface approaches the shear yield strength of the matrix. At higher levels of surface treatment there is a tendency for the shear strength to fall back. This may be due to "shearing off" of island platelets which stand proud on the heavily treated surface (cf. Marshall and Price [21]).

4.4. Pull-out tests

The parameters determined by the fits to the models will first be discussed. The values of q_0 are the same for each fibre type as the resin was constant and therefore the shrinkage stress would be the same.

The λ-values for each fibre are shown in Table V for the frictional-stress fit and these are similar despite the small data set at high embedded lengths. It is evident that there is little difference in surface roughness between the fibres, and this is consistent with the work of Robinson et al. [24] which showed no significant change in the surface area of the fibre until the equivalent of level 100. An average value of 1500 m^{-1} was adopted for λ for all the fibres in subsequent analysis. This leads to an estimate for the coefficient of friction of 1.25, which would seem to be rather high for the resin matrix against a smooth graphitic surface. If,

TABLE VI Surface acidity measurements from adsorption isotherms

Surface treatment level (C m^{-2})	Acidity (Mg) (μequiv g^{-1})	Acidity (Ag) (μequiv g^{-1})
0	6.4	5.9
10	8.9	
25	15.0	15.9
75	14.4	
100	17.2	15.1
400	15.6	

however, the debonding were cohesive, rather than interfacial, the friction would be between the two sides of a resin fracture. An additional check on this value can be obtained from the value of frictional shear stress, τ_f, determined from the frictional-stress plot, shown in Table IV, assuming this to be equal to μq_0 (ignoring the effects of Poisson contraction). From the value of q_0 in Table V we obtain a value of μ of 1.57, which is even higher than that obtained using the Hsueh model.

However, neither model considers the case of an anisotropic elastic fibre such as carbon and may, therefore, not fit in an exact manner. The parameters λ and σ were therefore rederived using an estimate of the actual transverse fibre modulus (~ 16 GPa) but this resulted in a change of only 4% in λ and only 3% in μ.

The results indicate a better fit to the model of Gao et al. above z_{max} and a good fit for the Hsueh model below z_{max}. However, as described by Kim et al. [18, 19], with an embedded length below z_{max}, the debond process is totally unstable and neither theory can be applied directly. The maximum debond stress is instead given by Equation 13 which is based on the assumption of unstable debonding [20].

It is proposed, therefore, that the debonding process may be considered to be *initiated* according to a shear-strength criterion. Failure of the interface will initiate in the region of maximum shear stress near the surface closest to the loaded end of the fibre. This must occur when some critical interfacial-shear strength is exceeded. It is also evident from the shear-strength criterion based on unstable debonding [20] that the longer the embedded length, the greater is the load needed to build up the shear stress to reach this interfacial-shear stress. If the embedded length is below z_{max}, then once the initial debonding has occurred the crack will propagate instantaneously in an unstable manner and complete debonding will occur, as in Fig. 7d. In this way, it is proposed that the initial part of the maximum debond-load–embedded-length plot can be described by Equation 13.

Under displacement-controlled conditions, once the crack tip is sufficiently far from either end, crack propagation is a stable process even in the absence of friction. Therefore, once the crack has been initiated, the model of Gao et al. may be applied to describe the crack tip, propagation behaviour. In the present case, which will reflect most practical situations, it is necessary to modify the model of Gao et al. in the following way to incorporate the initial unstable debonding

$$\sigma^* = \sigma_0 \exp(-\lambda l_z) + \bar{\sigma}(1 - \exp(-\lambda l_z)) \quad (19)$$

where the initial debond stress, σ_0, is given by Equation 13, and $l_z = L - z_{max}$ if $L \geqslant z_{max}$ and $l_z = 0$ if $L < z_{max}$. In other words, l_z is equal to the embedded length $L - z_{max}$ for lengths greater than z_{max}. Up to and including z_{max}, the expression above becomes equal to Equation 13 for unstable debonding. Above z_{max}, the expression becomes approximately equal to the model of Gao et al. but accounting for z_{max}.

The predictions of Equation 19 have been plotted on the maximum debond stress/embedded length axes

with the experimental data and an example is given in Fig. 11 for the level-25-treated fibre. There is better agreement than with either of the original models at all embedded lengths for all fibres, particularly for the stable failure mode.

It is now possible to reconsider those parameters which have been determined by the above modelling procedures. In fact all the values calculated for the individual models will hold. This is because the method used to calculate the constants in the model of Gao et al. by the delta-stress method considered only the embedded lengths above a changeover point which was found to have a similar value to z_{max}. In this way, only the data relevant to the model of Gao et al. where it was known to be valid was used to determine the parameters. The frictional stress plot is valid at all lengths since a varying initial stress is not included. Finally the shear-strength value for the Hsueh model was taken directly from the maximum debond data at low embedded lengths, and so it will be valid for lengths less than z_{max}.

4.5. General discussion

It is very difficult to compare the results of the fragmentation tests and the pull-out tests and attempts to analyse the differences have, so far, not been very successful. Both have disadvantages in that the results achieved are difficult to interpret and require stress analyses, they are also not representative of a real composite as they only deal with single fibres in resin, where $V_f \to 0$. Generally the pull-out test is considered to be more difficult experimentally, but additional information on shrinkage stresses and frictional coefficients are obtained. The fragmentation test, on the other hand, has been shown to provide additional information on the fibre strength.

The relation between the shear strengths, determined by both fragmentation tests and pull-out tests, and the fracture toughness of the interface and the acidity levels are shown in Fig. 12 and there is a clear trend towards higher strengths at the higher acidity levels. There is no reason to suppose that the relation should be linear but it is likely that there is a connection between acidity levels, the fracture toughness, G_{ic},
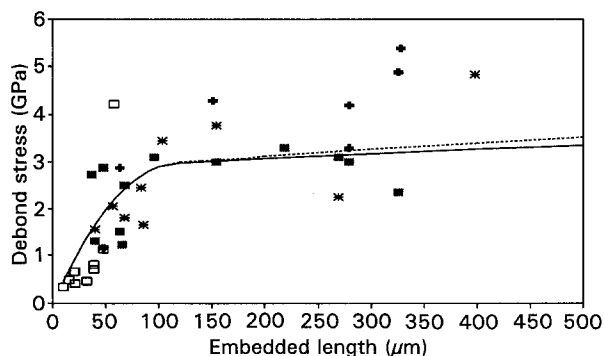

Figure 11 Maximum debond stress, τ_b, versus embedded length plot for fibre treated at the 25 C m^{-2} level showing the fit to (---) the modified Gao et al. model; (——) Hsueh model given for comparison. (■) Stable, (+) partially stable 1, (*) partially stable 2, (□) unstable.
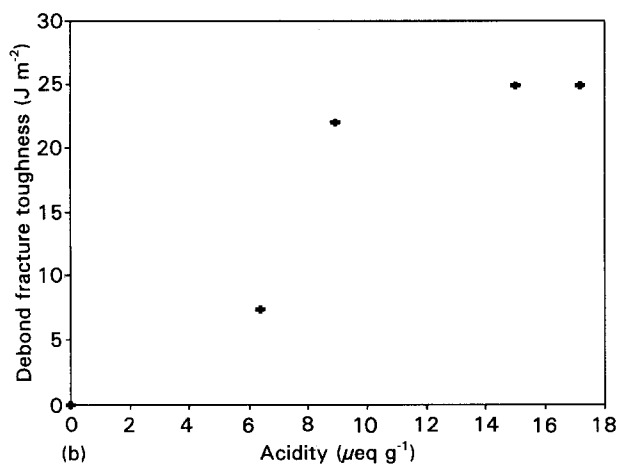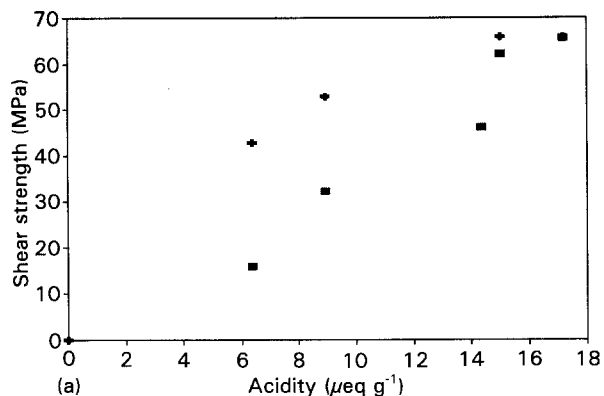
Figure 12 (a) The interfacial-shear strength, τ_i, from both (+) pull-out and (■) fragmentation tests, and (b) the debond fracture toughness, G_{ic}, from pull-out tests as a function of the surface acidity of carbon fibres.

TABLE VII A comparison of the components of the interfacial-shear strength

Surface treatment level $(C\ m^{-2})$	Friction stress, τ_f (MPa)	Fragmentation stress, τ_i (MPa)	Max debond stress, τ_b (MPa)
0	12.2	14	43
10	12.2	32.2	53
25	12.2	62.2	66
50	12.2	52.4	66
100	12.2	65.5	66

and bond strength, τ_b, as measured by pull-out tests, since these are all related to bond breaking. In fact, the correlation is better with the fragmentation-test shear strength, τ_i. This suggests that the value of τ_i for the treated fibres is also influenced by bond breaking and that it is little affected by friction.

The shear strengths generated from the pull-out test should be upper- and lower-bound values for the fragmentation-generated shear strengths. τ_b is a maximum value of the actual shear-stress distribution and it is not an average value, based on an elastic bond, and τ_f is an average frictional shear stress. In fact $\tau_f < \tau_i < \tau_b$ as is shown in Table VII. The fragmentation shear strength, τ_i, is an average calculated from a mixed-mode transfer length, as described above. It becomes more dependent on chemical bonding, creating elastic transfer, as the surface is treated by the electrolytic oxidation process.

It is difficult to show the possibility of the weak-layer effect graphically, and the interim levels between U and 10 have not been characterized in pull-out tests or for acidity. However, there is an obvious reduction in the shear strength at level 10 measured by the fragmentation test, which may be significant, as described above. It would appear that the adhesion mechanism with the treated fibre at the optimum treatment level, 25, is mainly by chemical bonding to acidic groups on the surface. It is likely that when this

type of bond is formed with the treated fibres that shrinkage pressure from the resin no longer makes any significant contribution to the bond strength. In the case of the untreated fibres, however, it plays the major role.

5. Conclusions

A high-strength, PAN-based carbon fibre was subjected to various levels of an anodic surface-treatment process. The process was found to be very effective in increasing the fibre–matrix interface strength as measured by the embedded-fibre fragmentation test and by a single-fibre pull-out test. Optimum surface treatment was achieved with a treatment of about $25\ C\ m^{-2}$ of fibre surface.

The tensile strength of the fibre, as measured in air and as estimated from the fragmentation test, was found to vary in a cyclic manner with the surface treatment. Strength peaks were observed at levels of 5–10 and $\sim 25\ C\ m^{-2}$. This is consistent with a model of removal of a weakly bonded surface layer from the fibre.

The fibre surface was characterized by chemi-adsorption and X-ray photoelectron spectroscopy (XPS). The acidity levels were considered to be due principally to the –COOH group and were found to rise with the surface treatment; they correlated well with the measured interface strengths.

A model for fibre pull-out is proposed which combines the principles of earlier models due to Gao–Mai–Cotterell and to Hseuh. Elastic behaviour occurs until a critical debond stress is exceeded at the fibre–matrix interface, thereafter a fracture-mechanics model is used to explain the form of the force–displacement trace observed during the test. In considering the data from both pull-out and fragmentation tests for the system studied, it is considered that in the case of untreated fibres, the interface strength is mainly frictional and it is controlled by the radial shrinkage stresses induced when the resin cures and is subsequently cooled to room temperature. On surface treatment a chemical bond involving the acidic sites on the fibre surface becomes dominant, and at the higher treatment levels friction plays a negligible role.

supply of fibre, Ciba Geigy for the resin, the RAE for the use of their surface treatment facility and pull-out testing equipment and Professor J. Castle and Dr J. Watts for helpful discussions regarding the adsorption isotherm studies.

References

1. W. W. WRIGHT, "Composite polymers" 3, edited by P. Dickin (RAPRA Tech. Ltd. Info. Pub., London, 1990) Part 1 p. 231, Part 2 p. 360.
2. L. C. WOLSTENHOLME and M. G. BADER, ICCM V111 Honolulu, edited by S. Tsai, G. Springer (SAMPE, Society for the Advancement of Materials Process Engineering, 1991).
3. H. D. WAGNER and A. EITAN, *Appl. Phys Lett.* **56** (1990) 1965.
4. B. YAVIN, H. E. GALLIS, J. SCHERF, A. EITAN and H. D. WAGNER, *Polym. Compos.* **12** (1991) 436.
5. M. J. PITKETHLY and J. B. DOBLE, "Interfacial phenomena in composite materials", Sheffield, edited by F. R. Jones (1989) p. 35.
6. G. DESARMOT and M. SANCHEZ, *Quatriemes Journees National sur les Composites* **4** (1984) 449.
7. J. C. FIGUEROA, T. E. CARNEY and L. S. SCHADLER, *Comp. Sci. Tech.* **42** (1991) 77.
8. D. A. CLARKE, PhD thesis, University of Surrey, UK (1988).
9. A. KELLY and W. R. TYSON, *J. Mech. Phys. Solids* **13** (1965) 329.
10. R. B. HENSTENBURG and S. L. PHOENIX, *Polym. Compos.* **10** (1989) 389.
11. A. N. NETRAVALI, P. SCHWARTZ and S. L. PHOENIX, *ibid.* **10** (1989) 385.
12. H. L. COX, *Brit. J. Appl. Phys.* **3** (1952) 72.
13. C. GURNEY and J. HUNT, *Proc. Roy. Soc. Lond A* **299** (1967) 508.
14. J. O. OUTWATER and M. C. MURPHY, Twenty-Fourth Annual Technical Conference on Reinforced Plastics/Composites Division SPI 11C (1970).
15. Y. C. GAO, Y. W. MAI and B. COTTERELL, *J. Appl. Maths. Phys (ZAMP)* **39** (1988) 550.
16. C. H. HSEUH, *Mater. Sci. Engng. A* **125** (1990) 67.
17. *Idem., ibid. A* **123** (1990) 1.
18. J. K. KIM, C. A. BAILLIE and Y. W. MAI, *J. Mater. Sci.* **27** (1991) 143.
19. *Idem., Scrip. Met. Mater.* **25** (1991) 315.
20. A. TAKAKU and R. G. C. ARRIDGE, *J. Phys. D. Appl. Phys.* **6** (1973) 2038.
21. P. MARSHALL and J. PRICE, *Composites* **22** (1991) 388.
22. E. KLINKLIN and M. GUIGON, Interfacial phenomena in composite materials, Leuven, edited by I. Verpoest and F. R. Jones (Butterworth-Heinemann, 1991) p. 83.
23. L. T. DRZAL, M. J. RICH and P. F. LLOYD, *J. Adhesion* **16** (1982) 1.
24. R. ROBINSON, S. LEHMANN, G. ASKEW, D. WILFORD, C. MEGERDIGIAN and R. PAPALIA, "High tech – the way into the 90's", edited by K. Brunsch, H. D. Golden and C. M. Herkert (Elsevier, 1986) p. 299.
25. P. DENISON, F. R. JONES and J. F. WATTS, *Sur. Int. Anal.* **20** (1985) 4647.
26. C. A. BAILLIE, J. F. WATTS and J. E. CASTLE, *J. Mater. Chem* (1991) in press.